Supporting Information

Ce doped NiOOH generated through electrocatalytic self-reconstruction of Ce doped Ni-MOF for efficient electro-oxidation of 5-hydroxymethylfurfural

Mingyue Dou,[a] Lele Gao,[b] Zhen Yan,[b] Hao Pan,[a] Zhiqiang Li,[c] Guangtong Hai,*[d] Xiubing Huang*[a]

[a] Advanced Innovation Center for Materials Genome Engineering, Beijing Key Laboratory of Function Materials for Molecule & Structure Construction, School of Materials Science and Engineering, University of Science and Technology Beijing, Beijing, 100083, P. R. China

[b] Rare Earth Advanced Materials Technology Innovation Center, Inner Mongolia Northern Rare Earth Advanced Materials Technology Innovation Co., Ltd., Baotou 014030, China

[c] Baotou Research Institute of Rare Earths, State Key Laboratory of Baiyunobo Rare Earth Resource Researches and Comprehensive Utilization, Baotou 014030, P. R. China

[d] Institute of Zhejiang University-Quzhou, Zhejiang University, 99 Zheda Road, Quzhou, Zhejiang Province 324000, P. R. China

* Corresponding author: haigt@zju.edu.cn (G. Hai), xiubinghuang@ustb.edu.cn (X. Huang)

Chemicals and Materials

All chemicals and materials were utilized exactly as received, with no further purification. Nickel nitrate hexahydrate [$Ni(NO_3)_2 \cdot 6H_2O$, AR] and acetone [C_3H_6O, AR] were purchased from Sinopharm Chemical Reagent Co., Ltd. Terephthalic acid [$C_8H_6O_4$, 99%] was purchased from Beijing InnoChem Science & Technology Co., Ltd. N,N-Dimethylmethanamide [DMF, AR] and hydrochloric acid [HCl, GR] was purchased from Beijing Tongguang Fine Chemical Co., Ltd. Cerium(III) nitrate hexahydrate [$Ce(NO_3)_3 \cdot 6H_2O$, 99.5%] was purchased from Thermo Fisher Scientific (China) Co., Ltd. 5-Hydroxymethylfurfural [HMF, 99.54%], furan-2,5-dicarbaldehyde [DFF, 98%] were purchased from Ark Pharma Scientific Co., Ltd. Potassium hydroxide [KOH, 95%], 5-hydroxymethyl-2-furancarboxylic acid [HMFCA, 98%], 5-formyl-2-furancarboxylic acid [FFCA, > 98%], 2,5-furandicarboxylic acid [FDCA, 98%] were purchased from Shanghai Aladdin Bio-Chem Technology Co., Ltd. Nickel foam [NF, 350 ± 25 g/m^2] was purchased from Beijing Tianmei Hechuang Technology Co., Ltd.

Synthesis

Scheme 1 illustrates the synthesis procedure for Ce-doped Ni-MOF. Initially, a nickel foam (NF) piece measuring 2 × 4 cm^2 was subjected to ultrasonic cleaning in 1 M HCl, acetone, and deionized water for 15 minutes each, followed by overnight drying in a vacuum oven. Subsequently, 1 mmol (0.2908 g) of $Ni(NO_3)_2 \cdot 6H_2O$ and 0.1 mmol (43.44 mg) of $Ce(NO_3)_3 \cdot 6H_2O$ were dissolved in 20 mL DMF under continuous stirring until transparent solution was obtained. In a separate container, x mmol (where x equals the total molar weight of nickel and cerium) of H_2BDC was dissolved in another 20 mL DMF solution, with 2 mL 0.25 M NaOH added dropwise during stirring. After 30 minutes, the ligand solution was rapidly poured into the metal salt solution. Following a 5-minute interval, the resulting transparent solution and the treated NF were transferred to a 50 mL Teflon reactor and maintained at 100 °C for 15 hours. The samples were then washed with DMF and ethanol and dried at 80 °C overnight. The final product was designated as NiCe(10%)-MOF. Other samples can be synthesized by adjusting the molar quantities of $Ce(NO_3)_3 \cdot 6H_2O$ and H_2BDC. The MOFs were subsequently activated via cyclic voltammetry (CV). In an electrolyte composed of 50 mM + 1.0 M KOH (or 1.0 M KOH), NiCe-MOF and Ni-MOF were subjected to CV for approximately 70 cycles within a potential range of 0.92-1.73 V_{RHE}. The resulting samples, after vacuum drying overnight, were labeled as NiCe-MOF-CV and Ni-MOF-CV, respectively.

Characterization

The morphology and microstructure were obtained by field emission scanning electron microscopy (FE-SEM, Hitachi SU8010, Japan) and transmission electron microscopy (TEM, JEM2200FS, Japan). The X-ray diffraction (XRD) patterns were acquired through a Bruker D8 ADVANCE with Cu Kα radiation (λ = 1.5406 Å) at 40 kV and 40 mA. X-ray photoelectron spectroscopy (XPS, Thermo Scientific ESCALAB 250Xi, USA) was used to collect information on elements in composite materials. Fourier infrared spectroscopy (FTIR, Nicolet 6700) was used to collect functional group information in composite materials. High-resolution Raman spectrometer (LabRAM HR Evolution) (325 nm) was used to study the structural evolution during electrochemical processes. The X-ray absorption fine structure (XAFS) was measured at room temperature on the BL14W1 baseline in the Shanghai Synchrotron Radiation Facility (SSRF). The elemental content was accurately characterized by inductively coupled plasma optical emission spectroscopy (ICP-OES, Agilent 5110 ICP-OES).

Electrochemical measurements

Utilizing a CHI-660D electrochemical workstation (CHI Instrument, Shanghai, China) in a typical three-electrode cell configuration, all electrochemical experiments were carried out at room temperature. A piece of the prepared self-supported catalyst, graphite rod, and Hg/HgO was applied as working electrode, counter electrode, and reference electrode, respectively. According to the Nernst equation, the measured potentials (vs. Hg/HgO) were stated concerning the reversible hydrogen electrode (RHE) scale: E (vs. RHE) = E (vs. Hg/HgO) + 0.098 + 0.0591 × pH. Before testing, the samples had to be activated using cyclic voltammetry (CV) to create stable curves. The working electrolyte for OER (or electrolysis) process and HMFOR process was 1.0 M KOH (pH = 14) and 50 mM HMF + 1.0 M KOH (pH = 14), respectively. Linear sweep voltammetry (LSV) curves with 90-iR compensation were collected at a scan rate of 5 mV s^{-1}. The Tafel plots of the catalysts were obtained by steady state timed current method. Different potentials (1.30 V_{RHE}-1.45 V_{RHE}) with a potential interval of 0.025 V_{RHE} were selected to test the current density. The current density at different potentials was used as the steady state current density (j_{ss}). The logarithmic value of steady state current density was plotted as the horizontal coordinate and the corresponding potential as the vertical coordinate. The in situ electrochemical impedance spectroscopy (EIS) curves were tested in the frequency range of 10^5 to 10^{-2} Hz with an AC amplitude of 5 mV at a specified voltage. Fitting the EIS

data produced the charge transfer resistance (Rct) and solution resistance (Rs). To determine the double layer capacitance (C_{dl}), CV curves taken at non-Faraday intervals (100, 80, 60, 40, and 20 mV s^{-1}) were utilized. Electrochemical surface area (ECSA) is computed using the following formula: ECSA = C_{dl} / C_s. Here, C_{dl} indicates the double-layer capacitance acquired from CV cycles, whereas C_s as specific capacitance of an ideal flat surface for Ni-based catalysts is 0.04 mF cm^{-2}.

HPLC analysis

High-performance liquid chromatography (HPLC, Agilent 1260 Infinity Series, USA) with an ultraviolet-visible (UV-Vis) detector and an Agilent Zorbax SB-C18 (150 mm × 4.6 mm, 5 μm) column was used to identify and quantify the substrate (HMF), intermediates (HMFCA, FFCA and DFF), and final oxidation product (FDCA). In a typical experiment, 50 μL of electrolyte was collected during potentiostatic electrolysis, diluted to 5 mL with deionized water, and analyzed using HPLC. In terms of analysis conditions, the UV-Vis detector had a wavelength of 265 nm. The mobile phases A and B were made up of chromatographic grade methanol and an aqueous solution of 5 mM ammonium formate, in a volume ratio of 3:7. The rate of flow was fixed at 0.6 mL min^{-1}. The column temperature was kept constant at 30 °C, and each separation lasted 10 minutes. To identify and quantify products, the external standard approach was utilized. This involved applying standard solutions with known concentrations of commercially available pure reactants, intermediates, and final products to obtain calibration curves.

The theoretical charge of the electrochemical oxidation reaction was calculated as follows:

$6 \times 10\ mM \times 8\ mL \times 96485\ C\ mol^{-1} = 46.3\ C$

Equations (1), (2), and (3) are used to calculate HMF conversion, FDCA yield, and Faradaic efficiency, respectively.

HMF conversation (%) = [n (HMF consumed) / n (HMF initial)] * 100 (1)

Product yield (%) = [n (certain product formed) / n (HMF initial)] * 100 (2)

Faraday efficiency (%) = [n (FDCA formed) / (charge/ (6*F))] * 100 (3)

where F denotes the Faraday constant (96485 C mol^{-1}) and n denotes the identified product's molar weight.

Computational methods

Based on the projection Enhanced wave (PAW) approach, the Vienna Atomic Number Simulation Package (VASP) is used for all spin polarization DFT computations. The electron-ion

interaction is described in terms of the conventional PAW potential. The plane wave base set is utilized to increase the wave function's smooth cross section with a 400 eV cutoff kinetic energy. A variant of the general gradient approximation (GGA), the Perdew-Burke-Ernzerhof (PBE) parameterization function is used during the electron-to-electron exchange and correlated interactions. The slab model was used to the surface in order to study the mechanistic chemistry of the surface process. To ensure good separation of periodic images, a sufficiently large vacuum area 15 is selected. In determining the properties of the surface, the bottom atoms are fixed in the body position during the geometric optimization process.

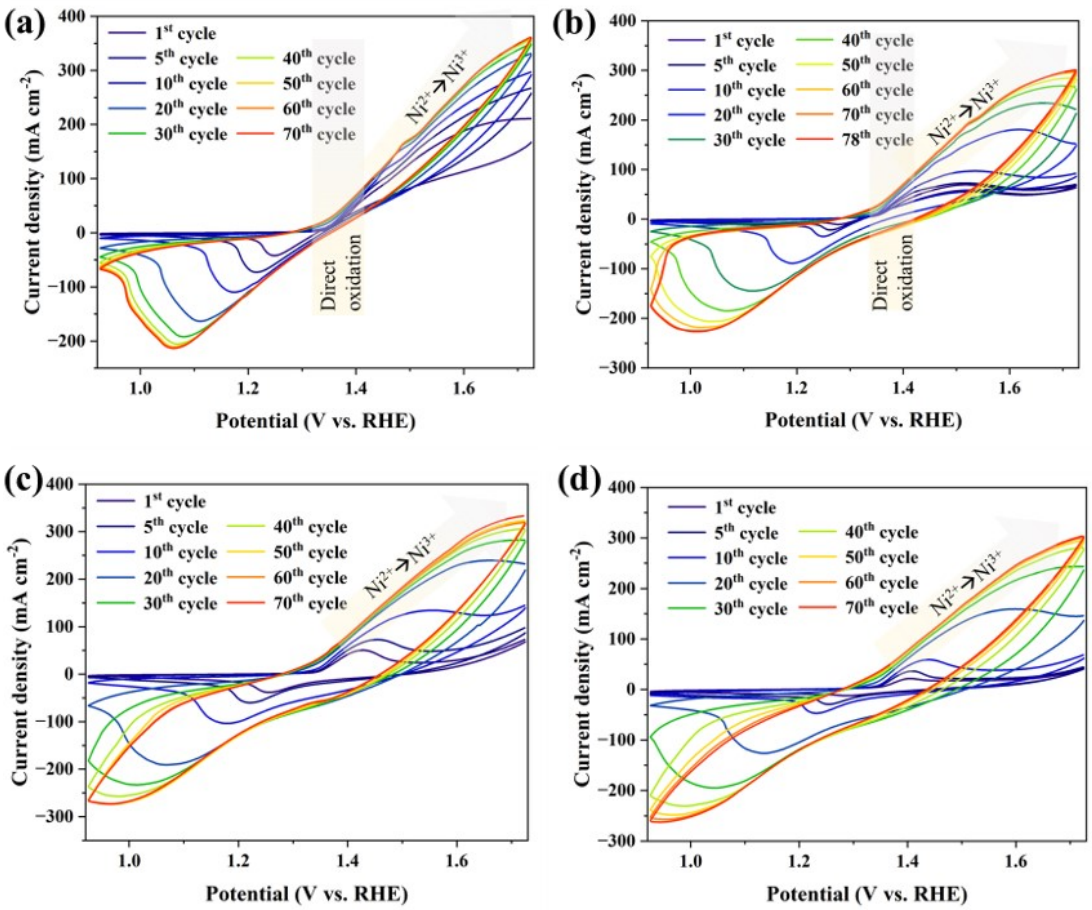

Figure S1. Detailed CV curves of (a) NiCe(10%)-MOF and (b) Ni-MOF in 50 mM HMF + 1.0 M KOH solution, (c) NiCe(10%)-MOF and (d) Ni-MOF in 1.0 M KOH solution.

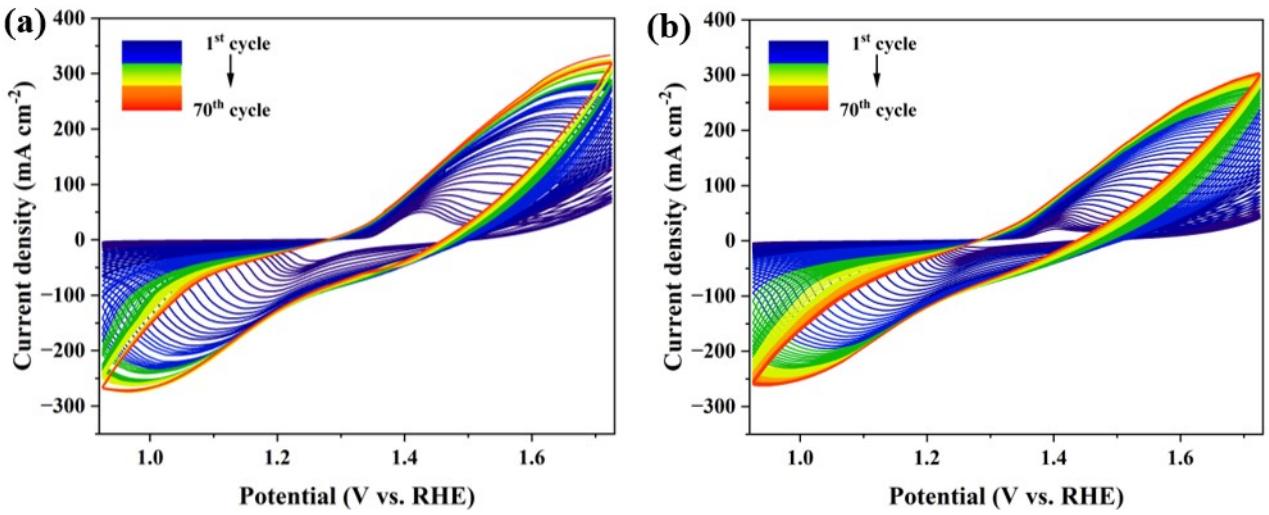

Figure S2. CV curves of (a) NiCe(10%)-MOF and (b) Ni-MOF in 1.0 M KOH solution.

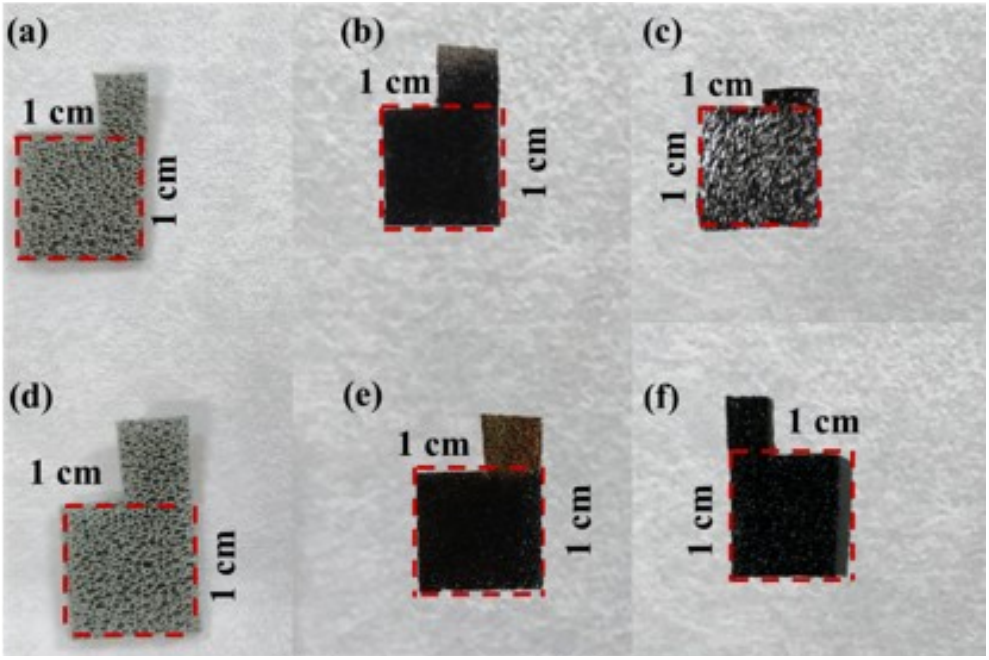

Figure S3. Optical photos of (a) Ni-MOF and (d) NiCe(10%)-MOF, (b) Ni-MOF-CV and (e) NiCe(10%)-MOF-CV in 50 mM HMF + 1.0 M KOH solution, (c) Ni-MOF-CV and (f) NiCe(10%)-MOF-CV in 1.0 M KOH solution.

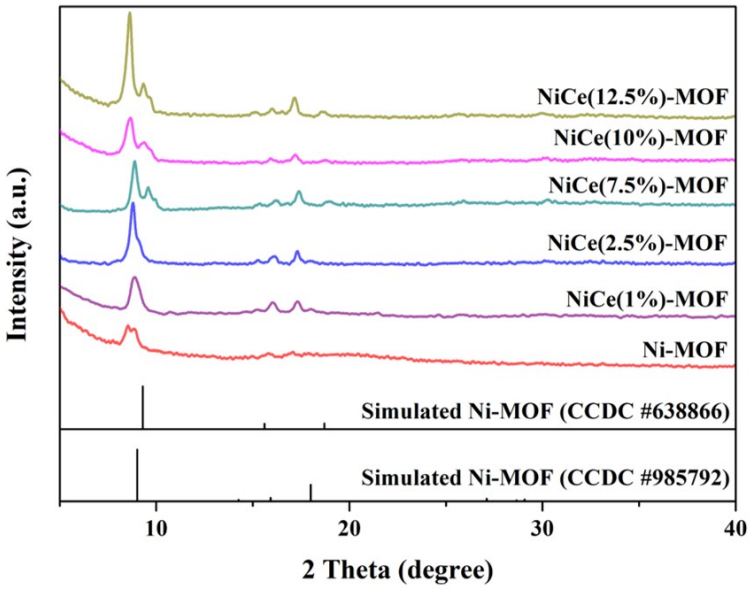

Figure S4. XRD patterns of varying ratio of NiCe-MOF.

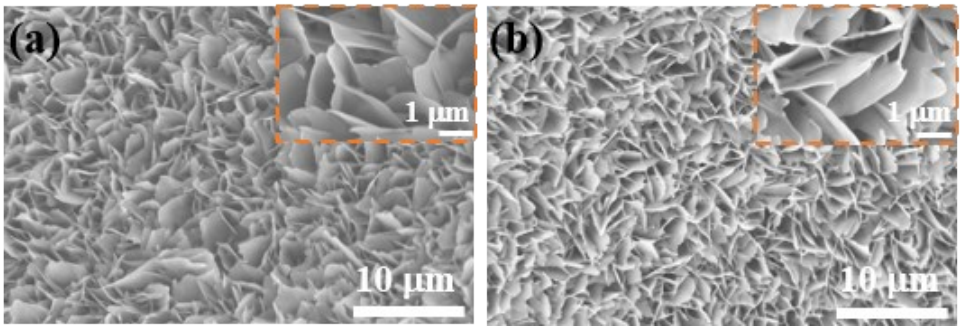

Figure S5. SEM images of (a) Ni-MOF and (b) NiCe(2.5%)-MOF.

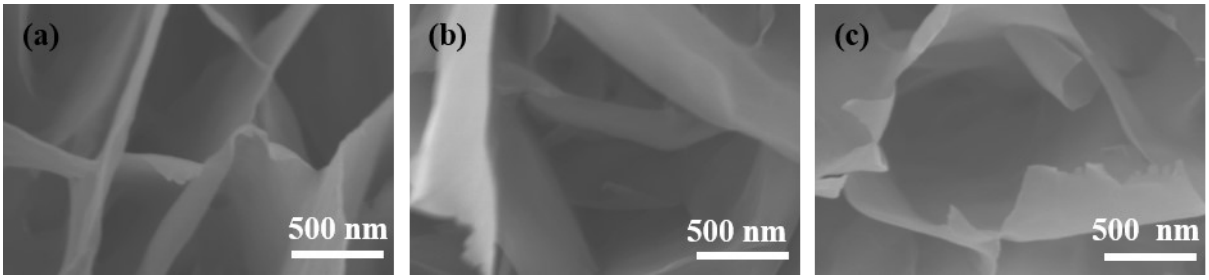

Figure S6. Higher magnification SEM images of (a) Ni-MOF, (b) NiCe(2.5%)-MOF and (c) NiCe(10%)-MOF.

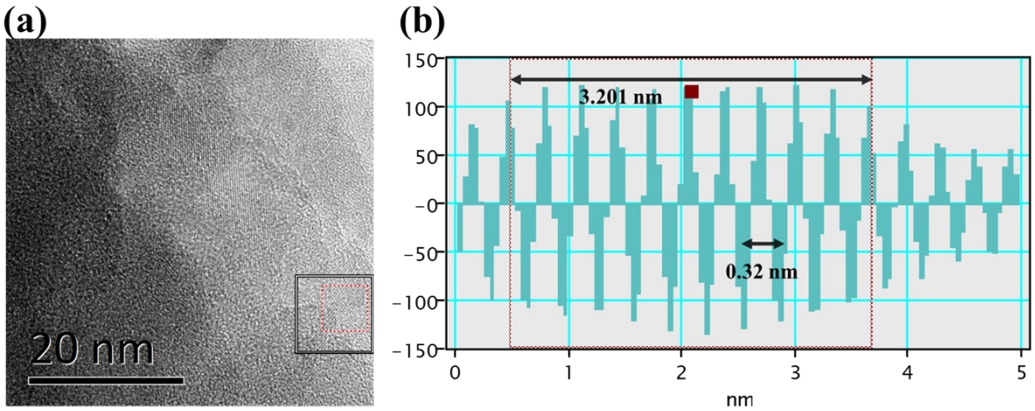

Figure S7. (a) HRTEM image and (b) the corresponding inter-planar spacing of Ni-MOF.

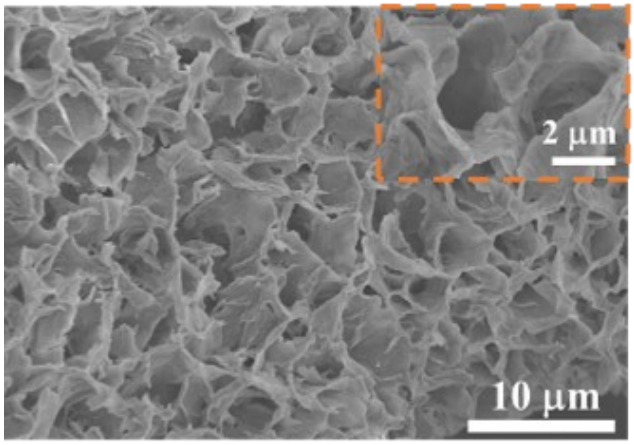

Figure S8. SEM image of Ni-MOF-CV.

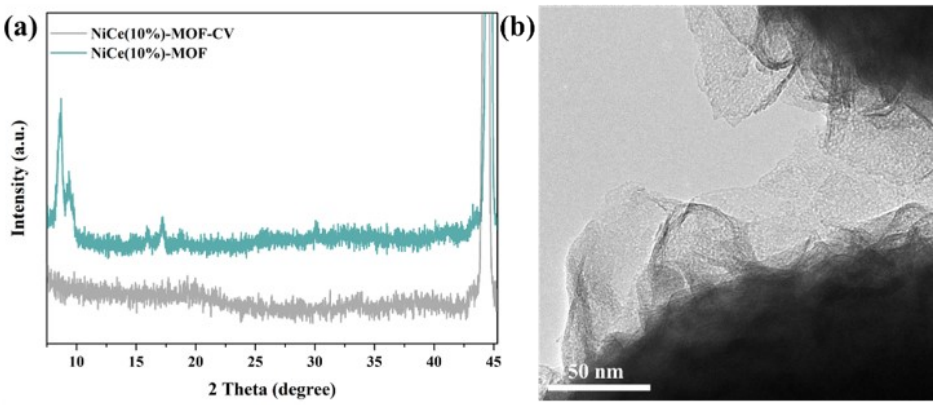

Figure S9. (a) XRD patterns and (b) TEM image of NiCe(10%)-MOF-CV.

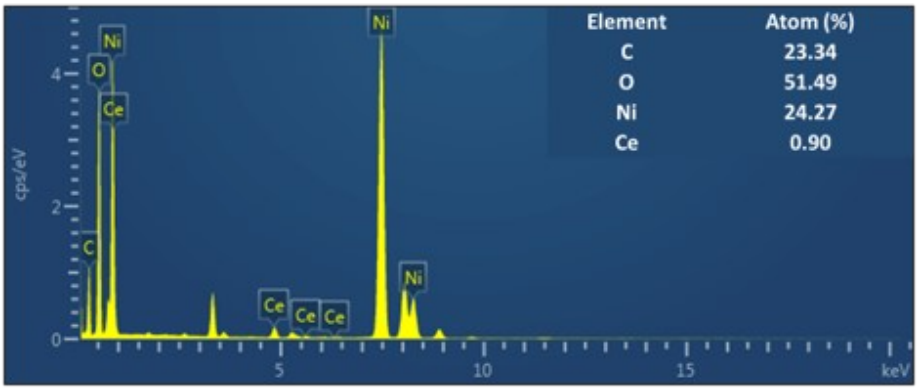

Figure S10. The relative element content of NiCe(10%)-MOF-CV.

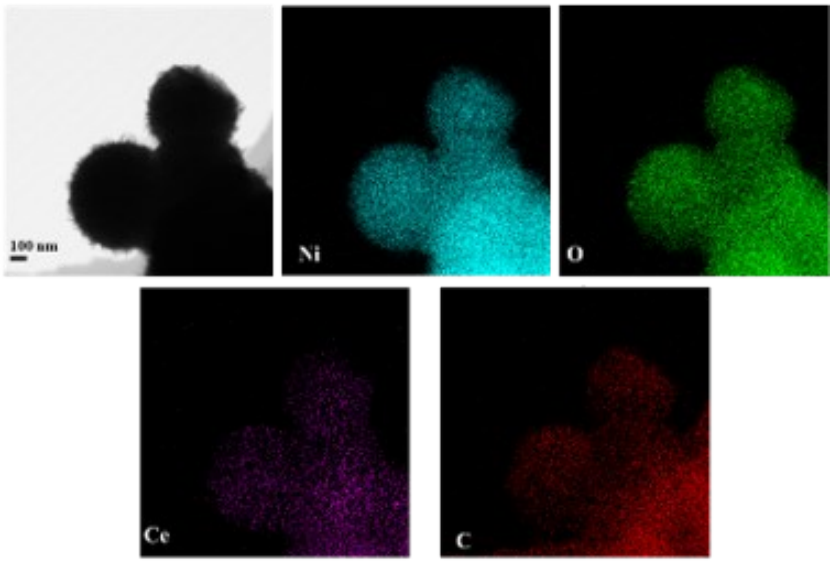

Figure S11. EDX mapping of NiCe(10%)-MOF-CV containing Ni, O, Ce, C.

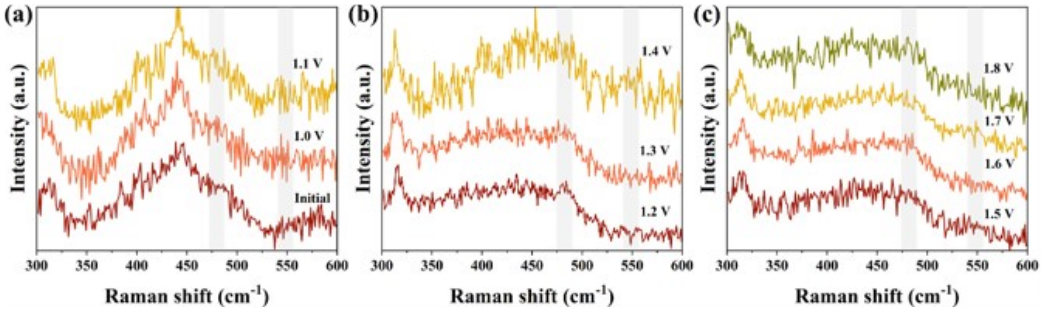

Figure S12. In-situ Raman spectroscopy of NiCe(10%)-MOF in 1.0 M KOH.

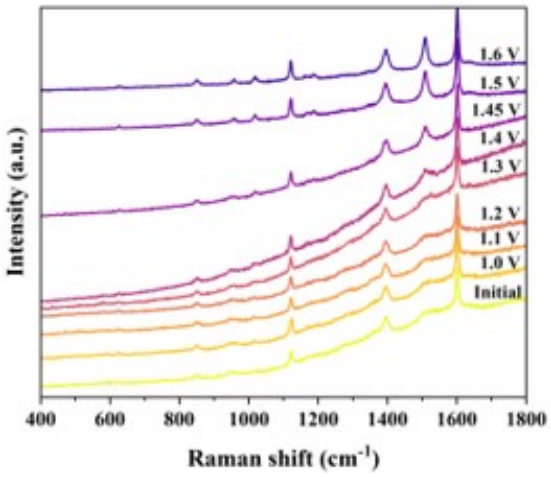

Figure S13. In-situ Raman spectroscopy of NiCe(10%)-MOF in 10 mM HMF + 1.0 M KOH solution.

Unlike the scenario where only 1.0 M KOH is present, the characteristic peaks of the MOFs were not weakened as the potential increased. This phenomenon may be attributed to the influence of other organic molecules, such as HMF. Additionally, the detection of characteristic peaks of NiOOH proved challenging, as the formed NiOOH is rapidly consumed and reduced back to $Ni(OH)_2$, coupled with the chemical oxidation of HMF.

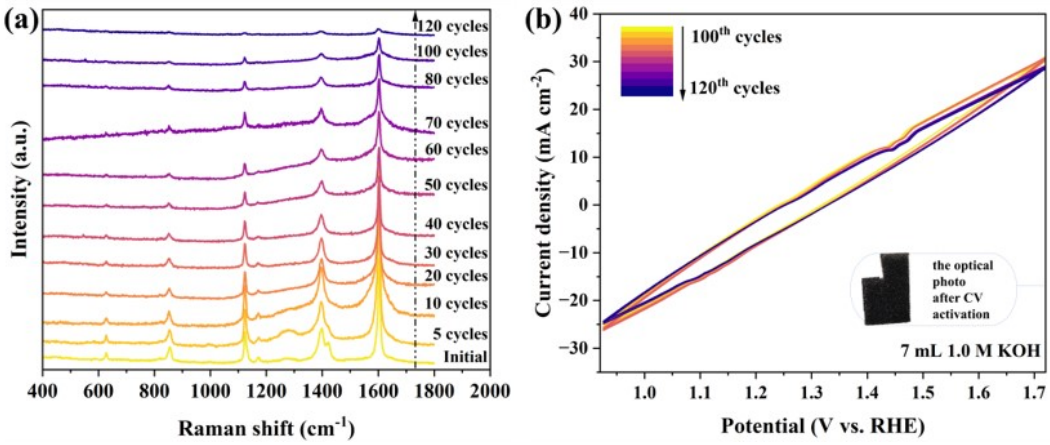

Figure S14. (a) In-situ Raman spectroscopy of NiCe(10%)-MOF in 1.0 M KOH during the CV process and (b) CV curves from 100th to 120th cycles and the optical photo of sample after CV activation.

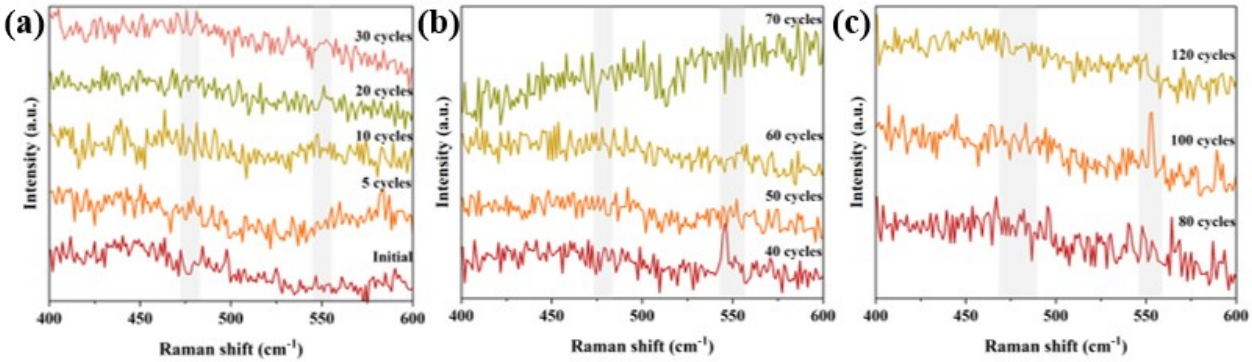

Figure S15. (a-c) In-situ Raman spectroscopy of NiCe(10%)-MOF in 1.0 M KOH from 0 to 120 cycles.

The in-situ Raman spectra of NiCe(10%)-MOF were recorded during CV activation to monitor structural changes in the catalyst. As shown in **Figure S14a**, NiCe(10%)-MOF exhibited characteristic MOFs signals (626, 852, 1122, 1397 and 1602 cm^{-1}), which gradually diminished upon successive CV test. Meanwhile, the black sample was observed after CV test (**Figure S14b**). Notably, after 40 cycles, weak characteristic peaks of NiOOH emerged (**Figure S15a-c**). Interestingly, while CV activation is typically completed within 70 cycles (as indicated in the **Figure S2a**), the MOFs-related peaks continue to diminish until 120 cycles in this experiment. This prolonged transformation may be attributed to differences in electrolyte volume.

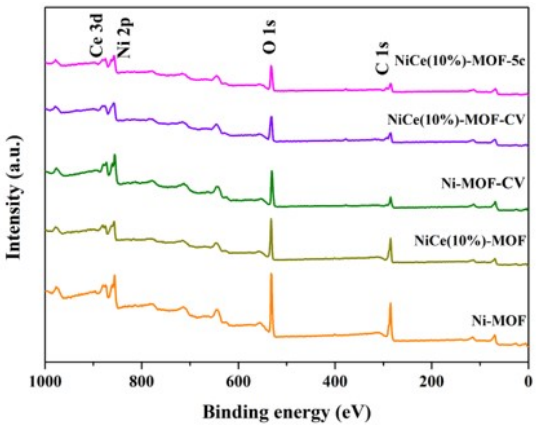

Figure S16. Full XPS spectra of Ni-MOF, Ni-MOF-CV, NiCe(10%)-MOF, NiCe(10%)-MOF-CV and NiCe(10%)-MOF-5c.

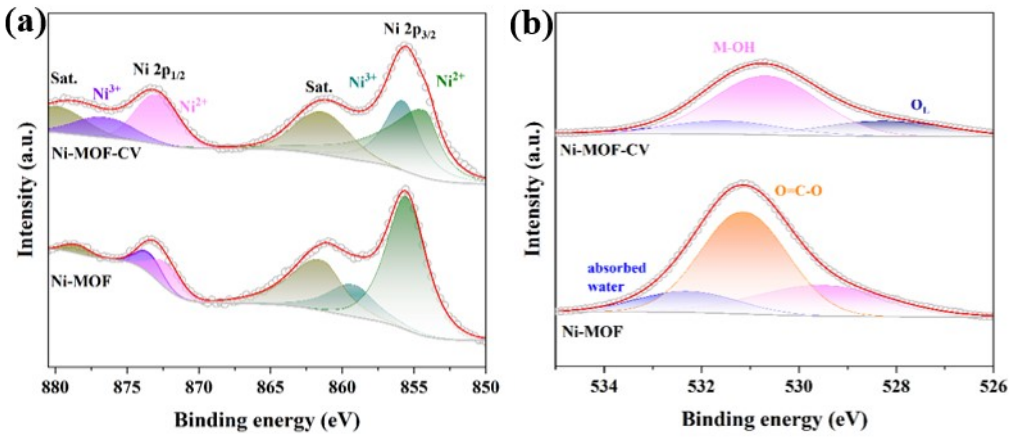

Figure S17. (a) High-resolution Ni 2p and (b) O 1s of Ni-MOF before and after CV activation.

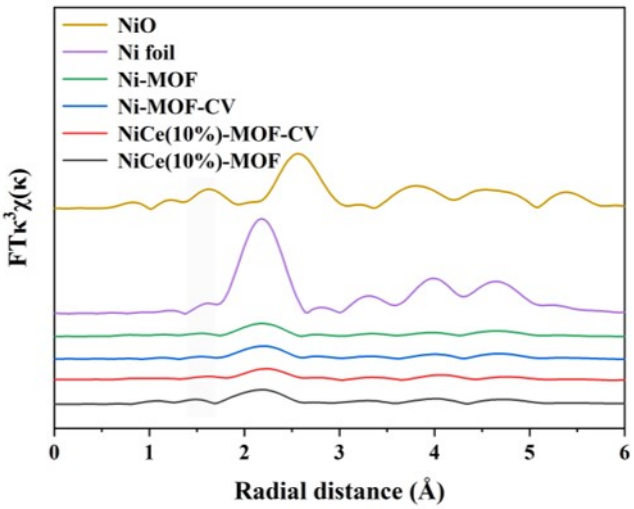

Figure S18. Ni K-edge of Fourier-transform extended X-ray absorption fine structure (EXAFS) of Ni-MOF, Ni-MOF-CV, NiCe(10%)-MOF, NiCe(10%)-MOF-CV, NiO and Ni foil.

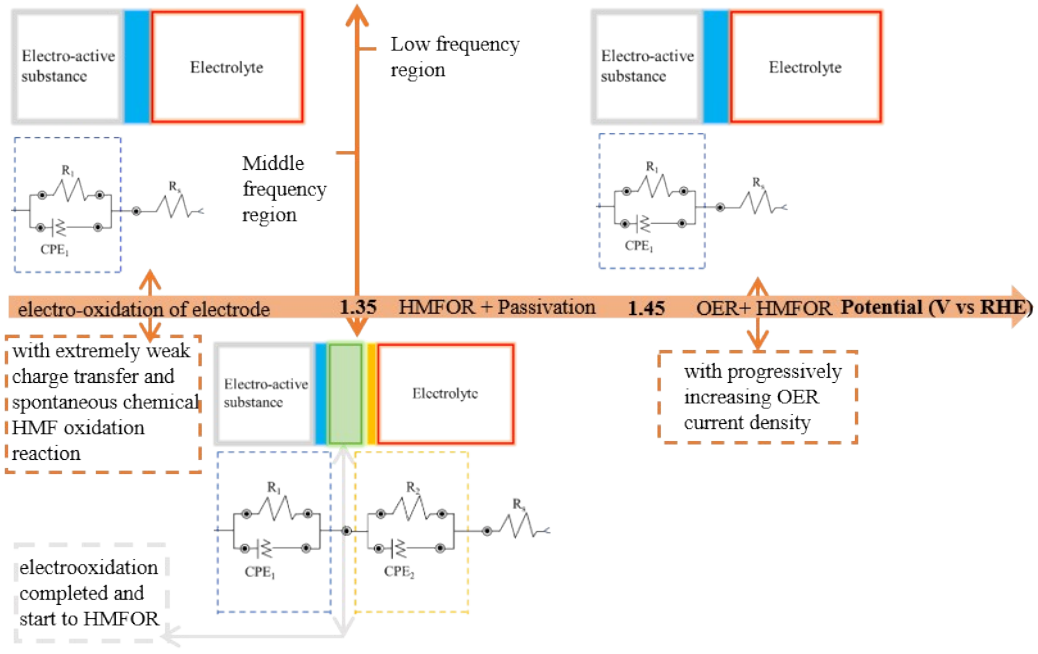

Figure S19. Schematic diagram of interface kinetics during complex electrochemical reactions for MOFs in 50 mM HMF + 1.0 M KOH.

Since the MOF has already been transformed into MOOH at the initial stage, the interface consists of the electroactive material and the electrolyte. Initially, in the mid-frequency region and at low potentials, both catalyst electrooxidation and chemical HMF oxidation occur. The electrooxidation process is not completed until reaching 1.35 V_{RHE}, at which potential electrochemical oxidation of HMF begins. Based on the obtained EIS raw data, two distinct interfaces are formed at this stage, which correspond to the Nyquist plot (two semicircles) and the Bode plot (two arch-shaped peaks). Beyond 1.4 V_{RHE}, the phase angle begins to increase, indicating the onset of passivation. Finally, when the potential reaches approximately 1.45 V_{RHE}, the oxygen evolution reaction (OER) takes place.

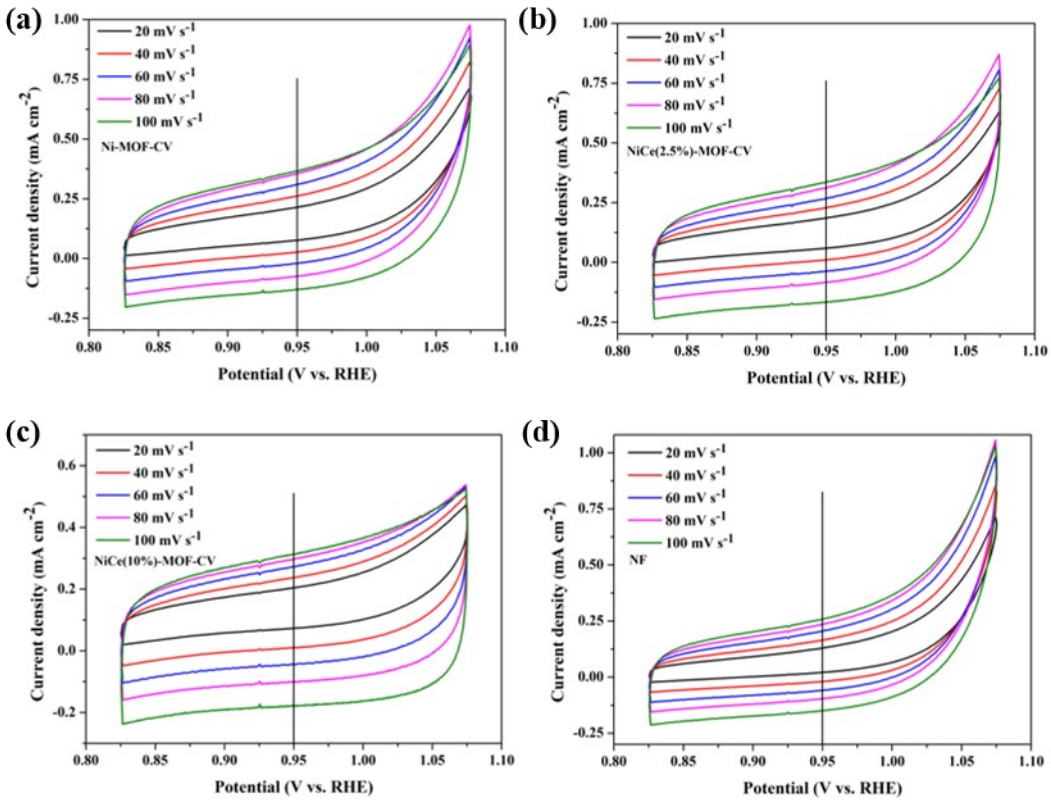

Figure S20. CV curves at 20, 40, 60, 80 and 100 mV s^{-1} for (a) Ni-MOF-CV, (b) NiCe(2.5%)-MOF-CV, (c) NiCe(10%)-MOF-CV and (d) NF in 50 mM HMF + 1.0 M KOH.

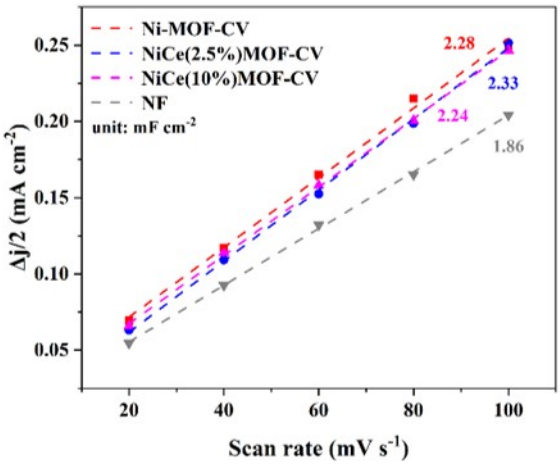

Figure S21. C_{dl} values of Ni-MOF-CV, NiCe(2.5%)-MOF-CV, NiCe(10%)-MOF-CV and NF in 50 mM HMF + 1.0 M KOH.

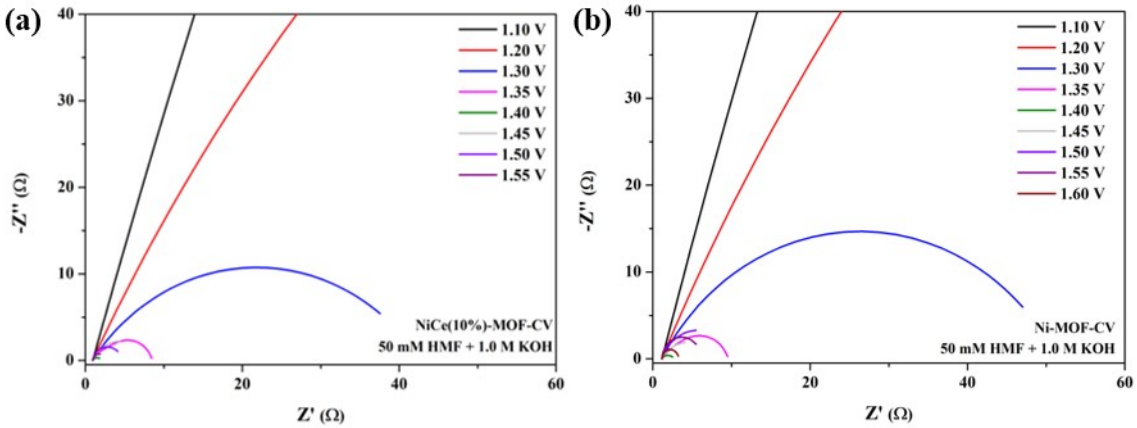

Figure S22. In situ Nyquist plots of (a) NiCe(10%)-MOF-CV and (b) Ni-MOF-CV in 50 mM HMF + 1.0 M KOH.

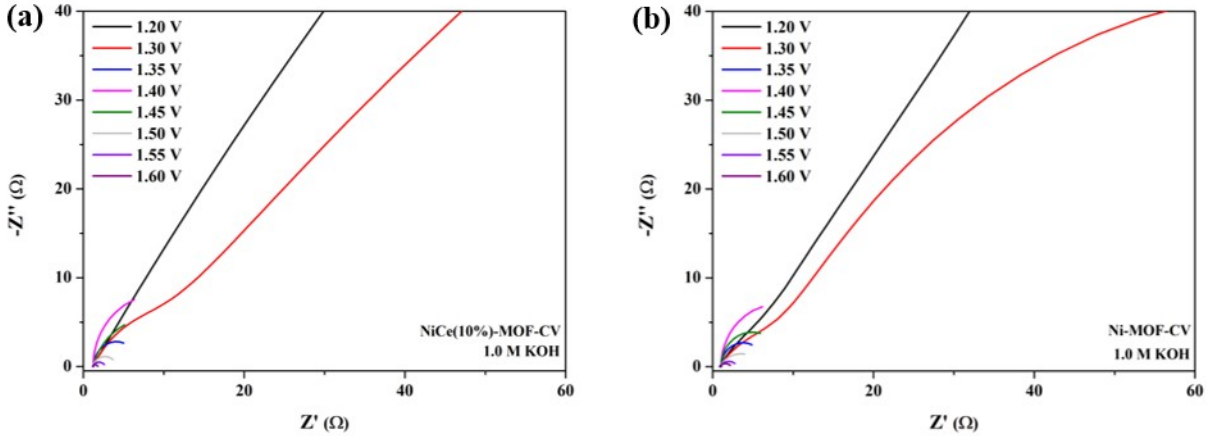

Figure S23. In situ Nyquist plots of (a) NiCe(10%)-MOF-CV and (b) Ni-MOF-CV in 1.0 M KOH.

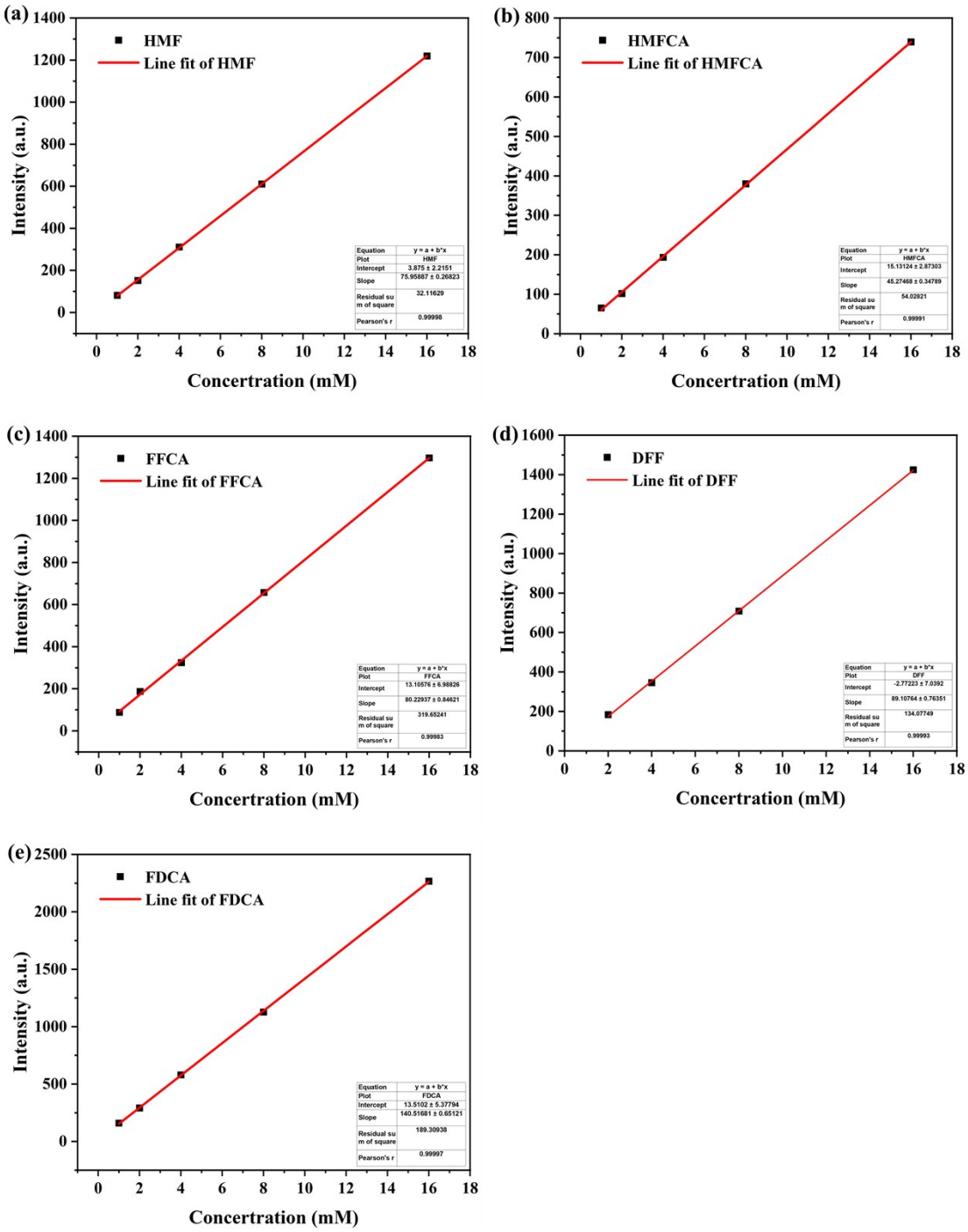

Figure S24. HPLC calibration curves for (a) HMF, (b) HMFCA, (c) FFCA, (d) DFF and (e) FDCA.

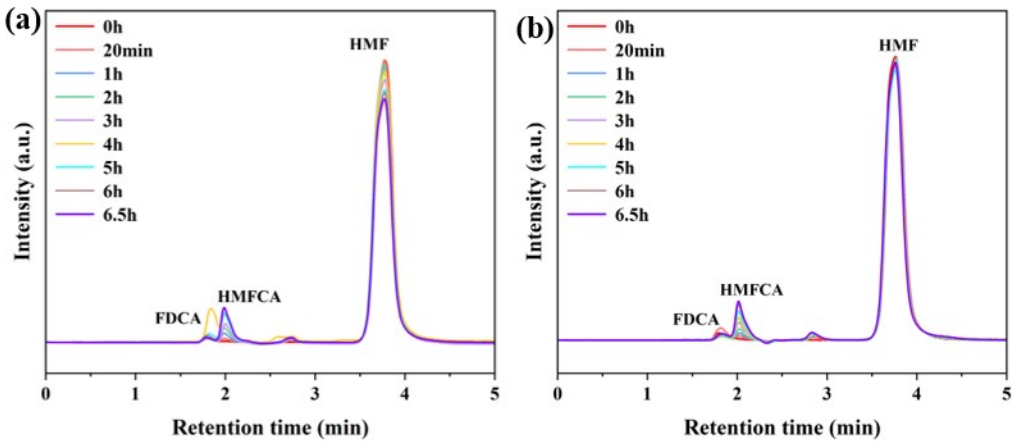

Figure S25. HPLC traces of the electrolyte (10 mM HMF + 1.0 M KOH with 20 mL KOH) without electrolysis (a) without stir and (b) with stir.

As shown in **Figure S25a**, the HMF conversion rate is 14%, with HMFCA and FDCA yields of 1% and 0%, respectively, after 6.5 hours. In **Figure S25b**, the HMF conversion rate is 4%, with HMFCA and FDCA yields of 2% and 0%, respectively, after the same duration. This phenomenon can be attributed to the inherent instability of HMF as an organic compound, which is highly susceptible to oxidation under alkaline conditions. The KOH solution, being a strong alkali, provides a high concentration of hydroxyl ions, thereby accelerating the oxidation of HMF. This process leads to the loss of hydrogen atoms from the hydroxymethyl and aldehyde groups of HMF.

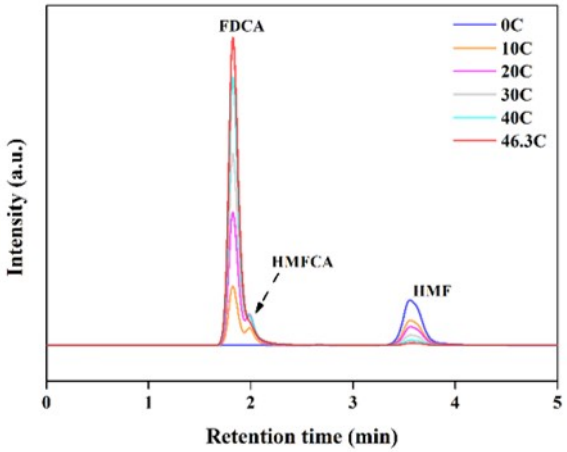

Figure S26. HPLC traces of electrolysis of HMF oxidation catalyzed by NiCe(10%)-MOF-CV at 1.44 V_{RHE} in 8 mL 10 mM HMF + 1.0 M KOH (each electrolysis lasts about 20 minutes).

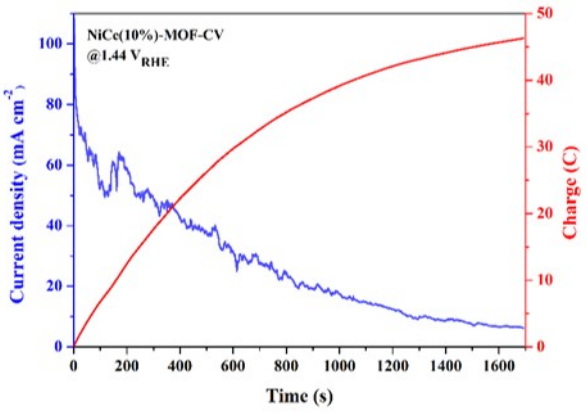

Figure S27. The current and charge versus electrooxidation time during HMF electrooxidation at 1.44 V_{RHE}.

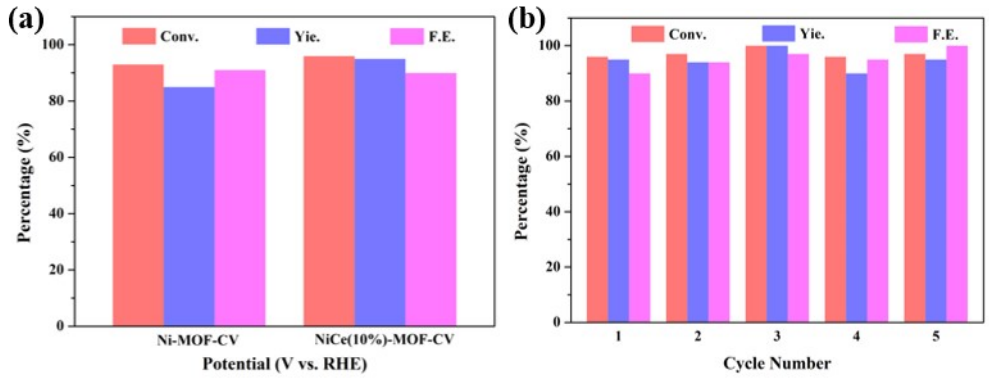

Figure S28. (a) Performance comparison between Ni-MOF-CV and NiCe(10%)-MOF-CV. (b) The HMF conversion, FDCA yield and Faradaic efficiency on NiCe(10%)-MOF-CV under 5 successive electrolysis cycles.

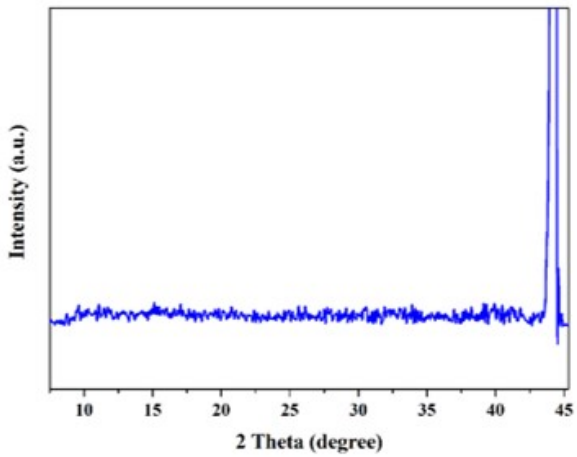

Figure S29. XRD patterns of NiCe(10%)-MOF-5c.

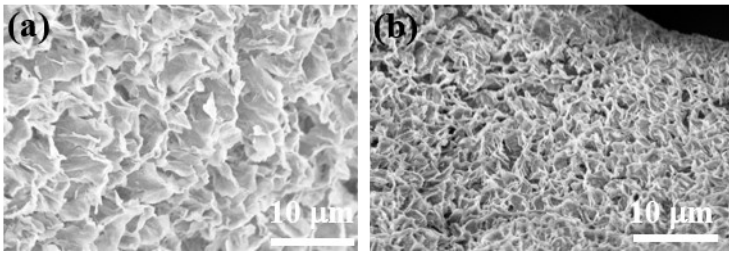

Figure S30. SEM images of (a) NiCe(10%)-MOF-5c and (b) NiCe(10%)-MOF-20c.

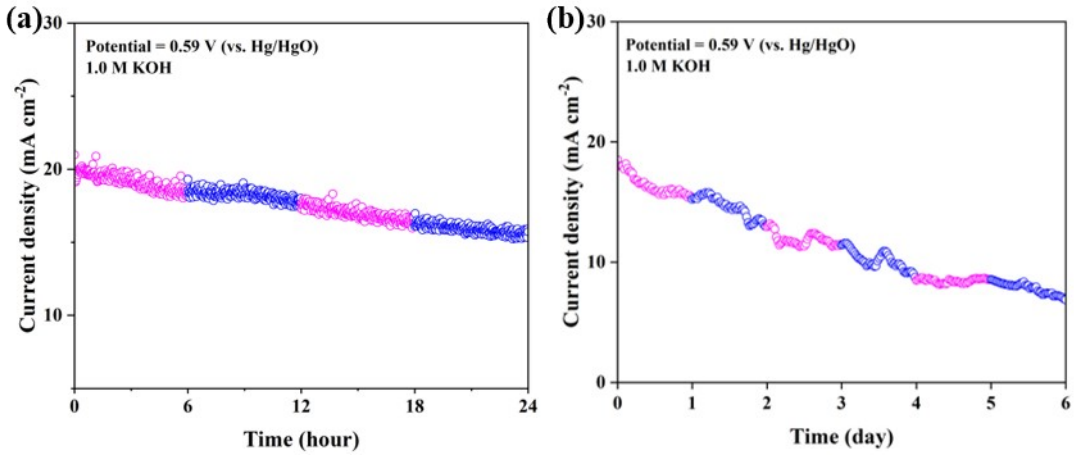

Figure S31. Current density-time curves of NiCe(10%)-MOF-CV under (a) 1 day and (b) 6 days in 1.0 M KOH solution.

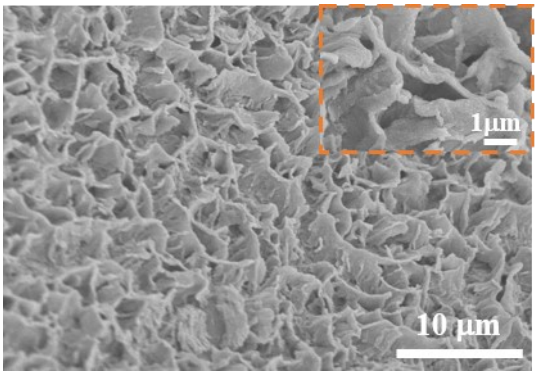

Figure S32. SEM image of NiCe(10%)-MOF-CV after 6-day stability test.

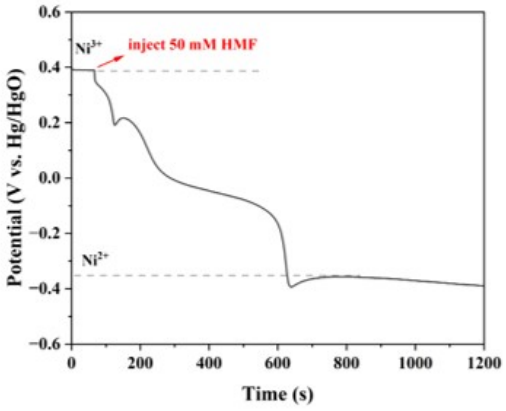

Figure S33. Open-circuit potential (OCP) measurement for NiCe(10%)-MOF-CV.

The catalyst was pre-oxidized in a 1.0 M KOH solution to form NiCe(10%)-MOF-CV, after which the open circuit potential (OCP) was recorded. Initially, the sample exhibited a stable state in the 1.0 M KOH solution. However, upon the addition of 50 mM HMF into the electrolyte, the open circuit potential rapidly decreased, signifying a significant disruption in the electrode potential equilibrium. This phenomenon can be attributed to the exchange of adsorbates and ions within the Helmholtz layer, suggesting a strong adsorption process of HMF on the surface. In the presence of 50 mM HMF, the NiOOH species is reduced to $Ni(OH)_2$ with a lifetime of approximately 10 minutes. This result demonstrates that NiOOH can rapidly react with HMF molecules.

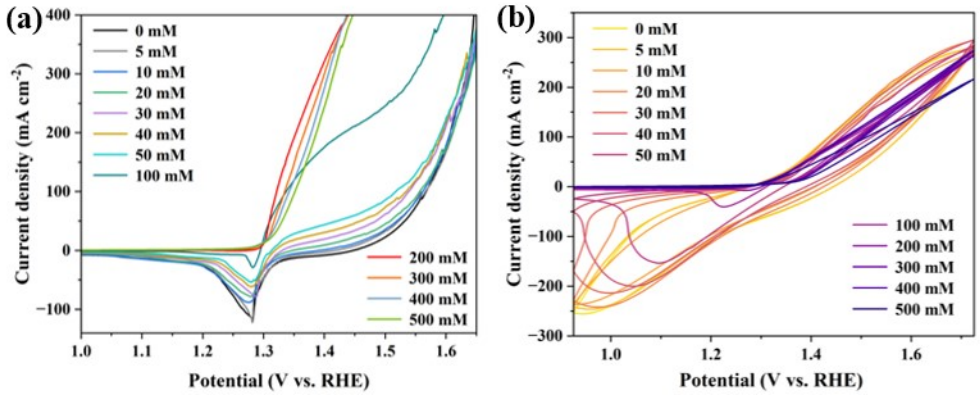

Figure S34. (a) LSV and (b) CV curves of NiCe(10%)-MOF in 1.0 M KOH electrolyte with different concentrations of HMF (0-500 mM).

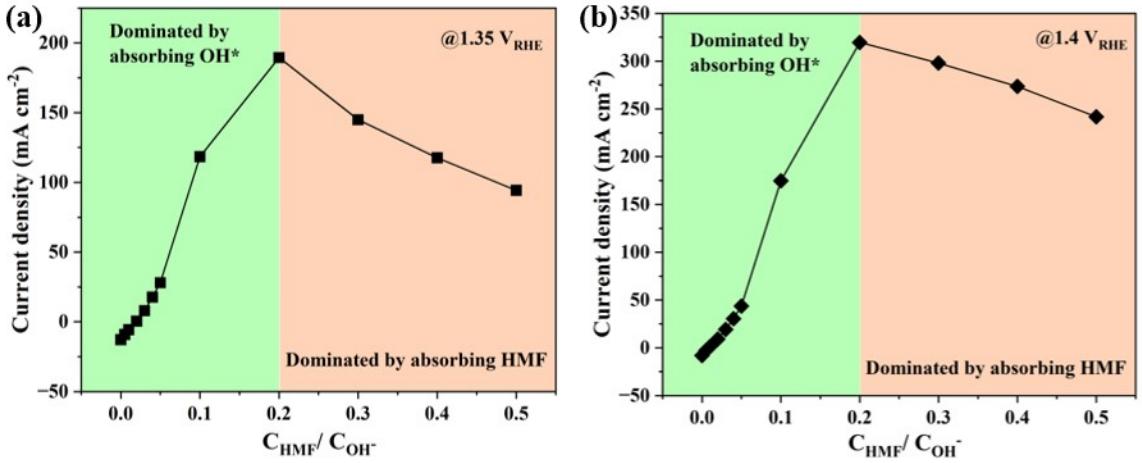

Figure S35. The relationship between current density with C_{HMF}/ C_{OH^-} at (a) 1.35 V_{RHE} and (b) 1.40 V_{RHE}.

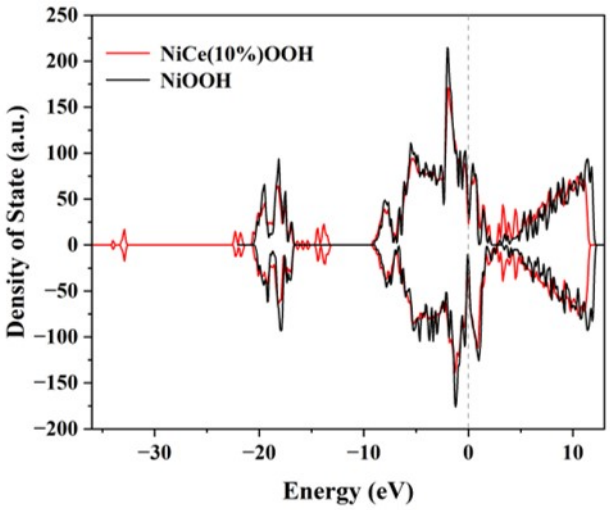

Figure S36. The electronic density of states (DOS) of NiCe(10%)OOH and NiOOH.

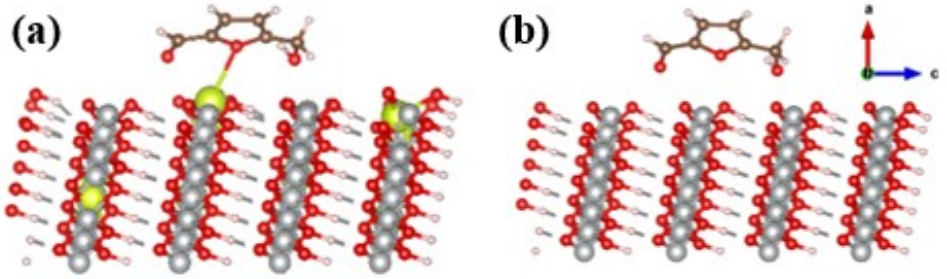

Figure S37. Adsorption configurations of the HMF on (a) NiCe(10%)OOH and (b)NiOOH (Ni atoms in grey, Ce atoms in yellow, O atoms in red and H atoms in white).

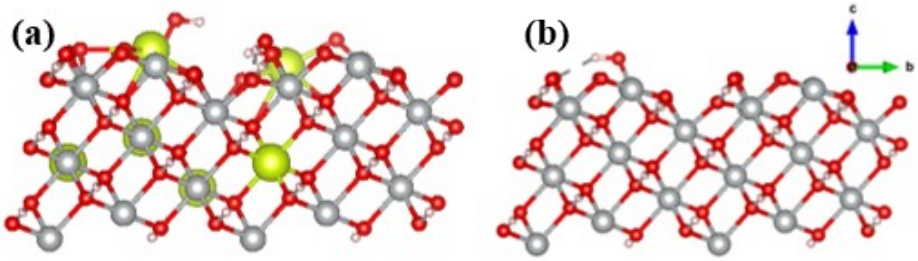

Figure S38. Adsorption configurations of the OH* on (a) NiCe(10%)OOH and (b) NiOOH (Ni atoms in grey, Ce atoms in yellow, O atoms in red and H atoms in white).

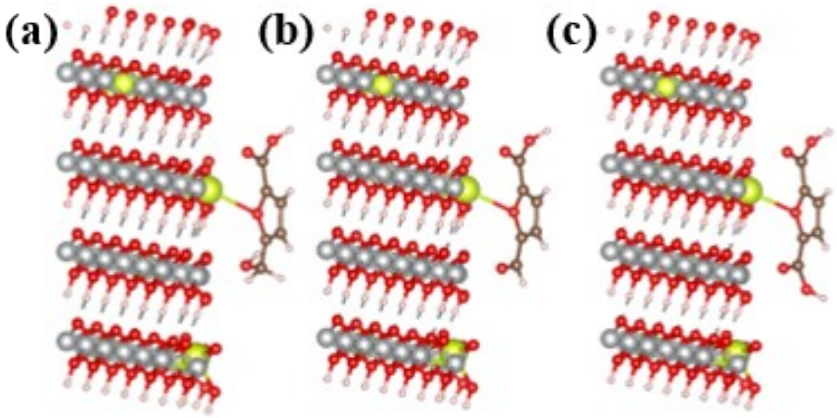

Figure S39. Adsorption configurations of HMFOR intermediates ((a) HMFCA (b) FFCA and (c) FDCA) on NiCe(10%)OOH.

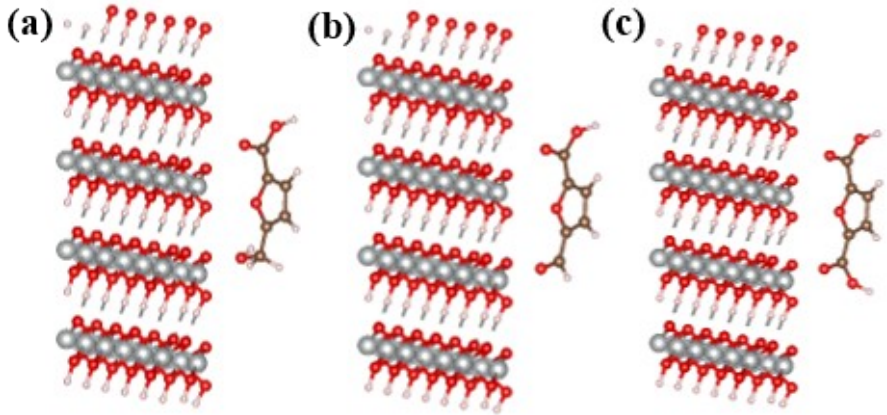

Figure S40. Adsorption configurations of HMFOR intermediates ((a) HMFCA (b) FFCA and (c) FDCA) on NiOOH.

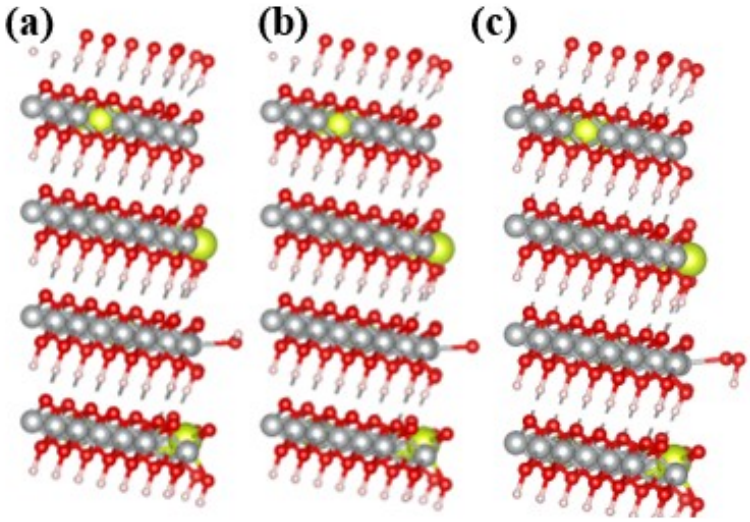

Figure S41. Adsorption configurations of OER intermediates ((a) OH* (b) O* and (c) OOH*) on NiCe(10%)OOH.

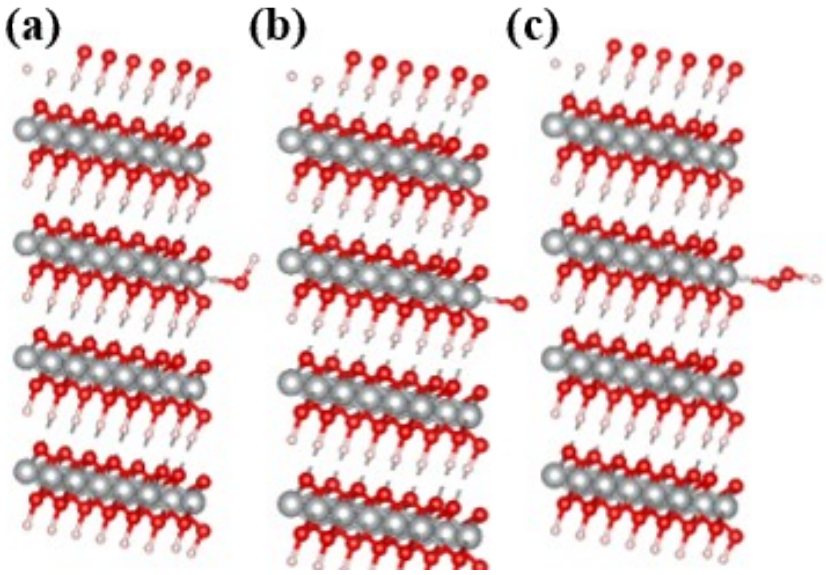

Figure S42. Adsorption configurations of OER intermediates ((a) OH* (b) O* and (c) OOH*) on NiOOH.

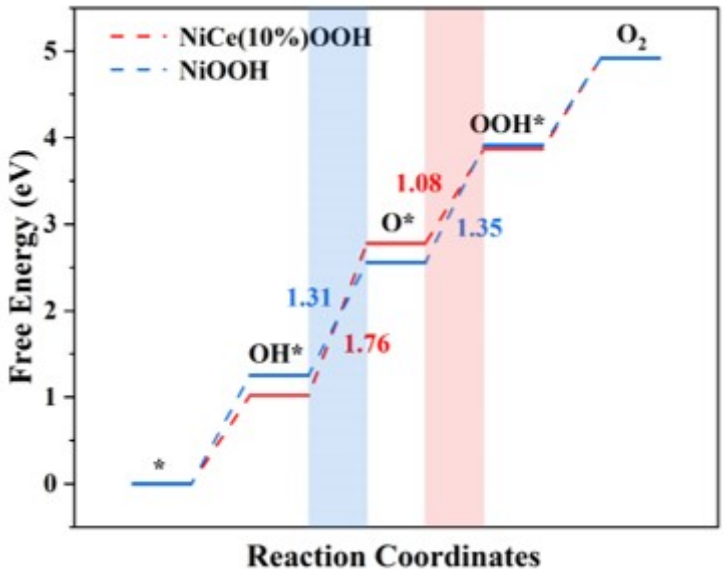

Figure S43. Free energy change during the OER process.

Table S1. The ICP results of various NiCe-MOF catalysts in this work.

Sample	Instrument Readings (mg/L)		Molar Percentage of Ce (%)
	Ni	Ce	
NiCe(2.5%)-MOF	21.9164	0.2236	0.4
NiCe(7.5%)-MOF	20.8032	3.638	7.3
NiCe(10%)-MOF	20.1151	4.530	9.4
NiCe(12.5%)-MOF	17.6821	5.1951	12.3

Table S2. The ICP results of various NiCe-MOF-CV catalysts in this work.

Sample	Instrument Readings (mg/L)		Molar Percentage of Ce (%)
	Ni	Ce	
NiCe(2.5%)-MOF-CV	18.6635	0.1984	0.4
NiCe(7.5%)-MOF-CV	19.3777	3.0743	6.6
NiCe(10%)-MOF-CV	19.7534	4.0190	8.5
NiCe(12.5%)-MOF-CV	20.0926	5.8214	12.1

Table S3. XPS peak types and corresponding binding energies of C 1s in as-prepared catalysts.

Element	Catalyst	C-C	O-C=O	C-O
C	NiCe(10%)-MOF	284.65 eV	288.16 eV	285.84 eV
	NiCe(10%)-MOF-CV	284.68 eV	287.86 eV	286.09 eV
	NiCe(10%)-MOF-5c	284.68 eV	288.38 eV	286.49 eV
	Ni-MOF	284.68 eV	288.48 eV	None
	Ni-MOF-CV	284.68 eV	288.62 eV	None

Table S4. XPS peak types and corresponding binding energies of Ni 2p in as-prepared catalysts.

Element	Catalyst	$2p_{3/2}$ ($Ni^{2+}$and Ni^{3+})	Satellite-1	$2p_{1/2}$ ($Ni^{2+}$and Ni^{3+})	Satellite-2
Ni	NiCe(10%)-MOF	856.45 eV 858.03 eV	862.76 eV	874.16 eV 876.12 eV	881.32 eV
	NiCe(10%)-MOF-CV	856.92 eV 859.32 eV	863.52 eV	875.23 eV 878.17 eV	882.59 eV
	NiCe(10%)-MOF-5c	856.26 eV 858.25 eV	863.57 eV	874.64 eV 877.13 eV	881.76 eV
	Ni-MOF	855.55 eV 859.17 eV	861.45 eV	872.21 eV 873.48 eV	878.45 eV
	Ni-MOF-CV	854.28 eV 855.73 eV	861.42 eV	872.90 eV 876.47 eV	879.84 eV

Table S5. XPS peak types and corresponding binding energies of Ce 3d in as-prepared catalysts.

Catalyst	Ce^{3+}		Ce^{4+}	
	$3d_{5/2}$	$3d_{3/2}$	$3d_{5/2}$	$3d_{3/2}$
NiCe(10%)-MOF	880.49 eV 884.25 eV	898.09 eV 903.15 eV	882.3 eV 893.84 eV 906.67 eV	901.2 eV 911.44 eV 924.27 eV
NiCe(10%)-MOF-CV	881.67 eV 884.91 eV	899.27 eV 903.81 eV	883.13 eV 895.99 eV 907.05 eV	901.44 eV 913.59 eV 924.65 eV
NiCe(10%)-MOF-5c	881.44 eV 885.09 eV	899.04 eV 903.99 eV	882.74 eV 895.32 eV 907.67 eV	901.64 eV 912.92 eV 925.27 eV

Table S6. XPS peak types and corresponding binding energies of O 1s in as-prepared catalysts.

Element	Catalyst	adsorbed H_2O	O-C=O	M-OH	O_L
O	NiCe(10%)-MOF	533.52 eV	531.76 eV	None	None
	NiCe(10%)-MOF-CV	533.80 eV	532.18 eV	531.14 eV	529.45 eV
	NiCe(10%)-MOF-5c	533.17 eV	531.77 eV	530.00 eV	529.03 eV
	Ni-MOF	532.28 eV	531.09 eV	529.53 eV	None
	Ni-MOF-CV	531.53 eV	None	530.68 eV	528.19 eV

Table S7. EIS fitting data at 1.35 V_{RHE} (two interfaces) in 1.0 M KOH with 50 mM HMF.

Sample	Rs	R_1	R_2	CPE_1-T	CPE_1-P	CPE_2-T	CPE_2-P
Ni-MOF-CV	1.099	7.79	1.181	0.050098	0.59614	0.2227	1.127
NiCe(2.5%)-MOF-CV	0.95916	7.303	2.951	0.034537	0.59537	0.27392	0.96287
NiCe(10%)-MOF-CV	0.89366	5.096	2.455	0.029186	0.65542	0.13125	1.07

Rs stands for the solution resistance, CPE_1 represents double layer capacitance, R_1 (Rct) has contact with the interfacial charge transfer reaction, CPE_2 and R_2 are related to the dielectric properties and the resistance of the electrode inner film.

Table S8. Comparison of activity between this work and other reported MOFs-based catalysts.

Electrode Materials	HMF (mM)	Potential (V vs. V_{RHE})	HMF conversion (%)	FDCA yield (%)	Faradaic efficiency (%)	Ref.
NiCoBDC-NF	10	1.55	-	99	78.8	J. Mater. Chem. A, 2020, 8, 20386-20392
NiFe	10	1.42	-	-	79.9	J. Mater. Chem. A, 2023, 11, 5527
CF-CuO/Ni-BTC MOF	10	0.55 V vs Ag/AgCl	100	99.9	91	Journal of Catalysis 417 (2023) 22–34
$Co(OH)_2$@ZIF-67	10	1.42	90.9	81.8	83.6	ACS Appl. Energy Mater. 2021, 4, 12909–12916
Rbf-Ni-MOF	10	0.8 V vs Ag/AgCl	-	-	95	Green Chem. 2022, 24, 9233–9244
Ni-CAT	10	1.42	-	98.7	86.8	ChemSusChem 2022, 15, e202101587
CF-Ni-MOF-Ag	10	1.623	~100	-	98.6	Appl. Surf. Sci. 2023, 608, 155152
NiCoFeS-MOF	50	1.39	100	99	99	J. Mater. Chem. A 2023, 11, 6375–6383
Ni-MOFs@$Ni(OH)_2$-NSs/NF	10	1.4	-	100	100	Chem. Commun., 2021,57, 11358
CoNiFe-MOFs/NF	10	1.4	-	99.76	100	J. Mater. Chem. A, 2021, 9, 14270
NiCe(10%)-MOF-CV	**50**	**1.44**	**100**	**98.6**	**99.8**	**This work**

Table S9. HPLC analysis of the HMF oxidation products on Ce doped NiOOH during 20 min.

Catalyst	HMF conversion (%)	FDCA yield (%)	HMFCA yield (%)
NiCe(10%)-MOF-CV	8%	2.4%	0.07%

To demonstrate the feasibility of chemical HMF oxidation, NiCe(10%)-MOF was activated in 1.0 M KOH to obtain NiCe(10%)-MOF-CV, which corresponds to the black Ce-doped NiOOH. The material was immediately immersed into the electrolyte without applying any potential. After stirring for 20 minutes, the product was analyzed using HPLC. The results revealed an FDCA yield of 2.4%, while almost no HMFCA was detected. Based on the control group results presented in **Figure S25**, as shown in **Figure S33** and **Table S9**, it is evident that NiOOH acts as an oxidant, enabling the spontaneous conversion of HMF to FDCA without the need for an applied potential, thereby confirming the occurrence of chemical HMF oxidation.